Journal of Materials Chemistry A

ROYAL SOCIETY OF CHEMISTRY

PAPER

View Article Online
View Journal | View Issue

Cite this: J. Mater. Chem. A, 2025, 13, 35547

Lightweight and ultra-flexible perovskite solar cells with a "sandwich" perovskite layer based on graphene–carbon nanotube electrodes

Mingming Li,[ab] Ying Yue,[ab] Di Zhang,[ab] Yuejuan Zhang,[ab] Yanchun Wang,[abd] Xiao Zhang,[abcd] Xiaojun Wei,[abcd] Huaping Liu[abcd] and Weiya Zhou[*abcd]

Flexible perovskite solar cells (FPSCs) have sparked widespread research enthusiasm due to their great potential in the booming fields of flexible electronics and portable devices. A lot of research has been conducted on the performance, flexibility, and stability of FPSCs, but the synergistic improvement of all three is still extremely difficult. In this work, we have achieved a lightweight and ultra-flexible perovskite solar cell (LWUF PSC) with high performance and remarkable stability. Specifically, in addition to using a 1.5 μm-thick polyetherimide film as a flexible substrate, the improved scheme mainly includes designing a "sandwich" architecture with multifunctionality to take advantage of perovskite quantum dots and polycrystalline perovskite, employing a flexible graphene–carbon nanotube film electrode, and a $CuCrO_2$ nanoparticle-based hole transport layer containing nickel to facilitate the transfer of photogenerated charge carriers. The resultant device demonstrates a stable power conversion efficiency (PCE) of 17.4% and a power-per-weight of 31.1 W g^{-1}. In particular, after 10 000 bending cycles with a curvature radius of 1 mm, the PCE of the LWUF PSC has sustained at 92.8% of its initial level, and after 32 days in an atmosphere with a relative humidity of 35%, it has remained at 93.0% of its initial level. The unique structural design of the device gives the LWUF PSC high PCE, significant power-per-weight, excellent mechanical flexibility and outstanding environmental stability, representing one of the best-performing LWUF PSCs to date without indium tin oxide electrodes.

Received 24th July 2025
Accepted 9th September 2025

DOI: 10.1039/d5ta06002h

rsc.li/materials-a

1. Introduction

Lightweight and ultra-flexible solar cells have great application potential as flexible and portable photovoltaic power sources, in both flexible electronics and aerospace.[1–3] However, current solar cells that combine high power conversion efficiency (PCE), light weight and flexibility often carry their respective shortcomings and cannot meet the requirements of practical use. For example, although the preparation process of high-performance solar cells based on Si and GaAs is technologically mature, the high-temperature process involved does not match the flexible substrate, so such devices usually form pseudo-flexible ones by integrating rigid structure units into the flexible substrate.[4,5] Organic solar cells, on the other hand, which are known for their high flexibility, currently have a low reported PCE of 10–15%.[6–8] Due to their excellent photovoltaic properties and compatibility with low temperature solution deposition, organic–inorganic halide perovskite based single-junction flexible perovskite solar cells (FPSCs) can achieve a high PCE of 22% on conventional flexible substrates,[9] and 12–20.2% PCE and 1.9–44 W g^{-1} power-per-weight on ultra-thin substrates.[1,10–18] The efficiency and power-per-weight significantly outperform those of other flexible cells, making perovskite-based structures ideal for future high-efficiency, lightweight and ultra-flexible solar cells.[19,20]

More importantly, mechanical robustness is the key criterion for evaluating the performance of FPSCs. Due to their poor flexibility and stability, the reported FPSCs fall far short of the requirements for practical use in portable devices.[21] For instance, the actual use of a FPSC will involve some bending, folding, and even slight stretching, which are poorly simulated by thousands of bending cycles at large bending radii. Moreover, in the previous flexibility experiments, the increased resistance of the flexible electrode and the large number of cracks in the perovskite film led to the rapid degradation of the FPSC's performance.[22] Thus, there is an urgent need to develop more flexible perovskite solar cells (PSCs) that can withstand rigorous mechanical testing under more demanding experimental conditions.

[a]Beijing National Laboratory for Condensed Matter Physics, and Institute of Physics, Chinese Academy of Sciences, Beijing, 100190, China. E-mail: wyzhou@iphy.ac.cn
[b]School of Physical Sciences and College of Materials Science and Optoelectronic Technology, University of Chinese Academy of Sciences, Beijing, 100049, China
[c]Songshan Lake Materials Laboratory, Dongguan, Guangdong, 523808, China
[d]Beijing Key Laboratory for Advanced Functional Materials and Structure Research, Beijing, 100190, China

Various schemes have been proposed to improve the deformation durability of FPSCs, such as reducing the substrate thickness,[23] replacing the conventional indium tin oxide (ITO) electrode with a highly flexible nanofilm or a highly conductive polymer electrode,[16,18,24] and improving the adhesion of each layer through interface engineering.[21,25,26] All of these strategies contribute to enhancing the mechanical stability of solar cells. Miao *et al.* prepared a FPSC with a PCE of ~12% on a silver nanowire electrode.[24,27] After 1000 bending cycles with a curvature radius of 1 mm, the PCE of the device remained above 99%. Unfortunately, the stability of the device was poor. The device's PCE had dropped to 81% of the initial value after 100 hours in a nitrogen-filled glove box. Recently, Hu *et al.*[28] fabricated a flexible $CsPbI_3$ quantum dot (QD) solar cell with the highest PCE of 12.3% assisted by introduction of the organic molecule phenyl-C61-butyric acid methyl ester (PCBM) into the $CsPbI_3$ QD layer, resulting in the formation of a hybrid heterojunction interfacial connecting layer. It should be noted that the target device is more flexible than the control polycrystalline perovskite cells, but it lost 30% of its initial efficiency after storage in a dry air-filled box for 14 days. In fact, poor stability is an obstacle for all PSCs. Particularly, this problem is exacerbated by the fact that the thinner polymer substrates in lightweight ultra-flexible devices have poorer moisture insulation compared to the glass substrates in rigid devices.[22] Accordingly, designing high efficiency, lightweight, and ultra-flexible devices must be combined with optimizing the device's stability for realizing the real application of FPSCs as flexible and portable photovoltaic power sources. Therefore, synergistically improving the efficiency and stability for lightweight, ultra-flexible PSCs (LWUF PSCs) remains a formidable challenge.

In this work, through comprehensively considering several key influencing factors (such as substrate thickness, electrode, and interface), we demonstrate a LWUF PSC with high performance and excellent stability by adopting a collaborative approach to improve the performance of the FPSC. Specifically, a freestanding, super-light, remarkably flexible and highly transparent conductive graphene–carbon nanotube (G-CNT) nanofilm is selected as the electrode to replace the conventional oxide electrode; an ultra-thin (1.5 μm-thick) polyetherimide (PEI) film is used as the flexible substrate; the hole transport layer (HTL) is optimized to improve the PCE of the FPSC; and the perovskite absorbing layer is designed for the first time to use a "sandwich" architecture composed of $CsPbBr_3$ QDs/polycrystalline perovskite mixed $CsPbBr_3$ QDs/$CsPbBr_3$ QDs. In this "sandwich" layer, the nanoscale perovskite QDs occupy the bulk polycrystalline perovskite grain boundaries and the surfaces to form a multi-scale hybrid interface of QDs wrapped around polycrystalline grains, achieving efficient charge transfer and mechanical flexibility, by combining the advantages of nano-scale perovskite QDs and polycrystalline films. As a result, our approach synergistically improves the performance of LWUF PSCs, achieving a high PCE of 17.4% and a power-per-weight of 31.1 W g^{-1}, excellent mechanical stability (maintaining 92.8% of the initial PCE after 10 000 bending cycles with a curvature radius of 1 mm), and marked environmental stability (maintaining 93.0% of the initial PCE after 32 days under ambient conditions).

2. Experimental section

2.1 Materials

Lead(II) iodide (PbI_2, 99.9985%) and copper foil (99.8%) were purchased from Alfa Aesar. Cesium iodide (CsI, 99.999%), lead bromide ($PbBr_2$, 99.99%), cesium carbonate (Cs_2CO_3, 99%), chromium(III) nitrate nonahydrate (99.99%), copper(II) nitrate trihydrate (99.99%), nickel nitrate (99.99%), 2,9-dimethyl-4,7-diphenyl-1,10-phenanthroline (BCP, 98%), chlorobenzene (CB, 99.8%), *N*,*N*-dimethylformamide (DMF, 99.9%), dimethyl sulfoxide (DMSO, 99.9%), 1-octadecene (90%), methyl acetate (99%), oleic acid (85%), oleylamine (80–90%) and *n*-hexane (99%) were purchased from Beijing InnoChem Science & Technology Co., Ltd, China. Methylamine hydrochloride (MACl, 99%) was purchased from Acros. Formamidine hydroiodide (FAI, 99.99%) and poly(3,4-ethylenedioxythiophene)–poly(-styrenesulfonate) (PEDOT:PSS, 1.5%) were purchased from Shanghai Aladdin Biochemical Technology Co., Ltd, China. PCBM (99%) was purchased from Xi'an Polymer Light Technology Corp., China. PEI was purchased from Suzhou Diamond Electronic Technology Co., Ltd, China.

2.2 Synthesis of G-CNT films, $CuCrO_2$(Ni) nanoparticles and $CsPbBr_3$ QDs

The G-CNT films were synthesized on copper (Cu) foils using a low-pressure chemical vapor deposition system.[29] The process steps are as follows: first, the freestanding carbon nanotube (CNT) films were grown directly and continuously by the blown aerosol chemical vapor deposition method, according to our earlier report.[30] A piece of freestanding CNT film was first transferred onto a pre-polished Cu foil and then placed in the quartz tube inside a furnace (OTF-1200X). The system was evacuated and then heated to 900 °C. After annealing in H_2 for 30 min, the system was heated to 1040 °C, and CH_4 (purity: 99.999%) gas at a 1 sccm flow rate was introduced into the system to grow graphene. After 30 min, the system was turned off and cooled to room temperature. Finally, G-CNT/Cu foil was cut into 2.5 cm × 2.5 cm pieces and dipped into $FeCl_3$ solution to dissolve the Cu foil and then rinsed in water and ethanol solution to obtain a pure freestanding G-CNT film. Using chromium nitrate, copper nitrate and nickel nitrate as precursors, at a molar ratio of 5 : 5 : 1, copper–chromium oxide nanoparticles containing nickel were prepared by a hydrothermal method similar to that reported previously.[31,32] The structural characterization showed that the synthesized nanoparticles exhibit a 2H–$CuCrO_2$ crystal structure (Fig. S1a); therefore, it was labeled as $CuCrO_2$(Ni). $CsPbBr_3$ QDs were synthesized by a heat injection method and alternately purified using methyl acetate and *n*-hexane as reported previously.[33]

2.3 Fabrication of solar cells

2.5 cm × 2.5 cm glass and PEI substrates, as well as a glass/ITO electrode substrate, were cleaned using an ultrasonic cleaner

with detergent, deionized water, acetone, and isopropanol for 20 min each. Before use, the above substrates were dried with air and treated with a plasma cleaner for 5 min. For ultra-thin PEI/G-CNT electrode substrates, poly(dimethylsiloxane) (PDMS, Sylgard 184) and its curing agent (mass ratio 10 : 1) were spin-coated onto dried glass at 4000 rpm for 1 min and then dried at 80 °C for 50 min, and then a 1.5 μm-thick PEI film was attached to the glass/PDMS rigid substrate; finally, the pure freestanding G-CNT film obtained in section 2.2 was directly laid out on the PEI film. After further drying, the G-CNT film and PEI film were firmly adhered together under the action of surface van der Waals force. Subsequently, a PEDOT:PSS or $CuCrO_2$(Ni) HTL was deposited on this glass/PDMS/PEI/G-CNT structure by the spin-coating process. For the PEDOT:PSS HTL devices, PEDOT:PSS was spin-coated at 4000 rpm for 40 s and then annealed at 120 °C for 40 min. For $CuCrO_2$(Ni) HTL devices, a 5 mg mL^{-1} $CuCrO_2$(Ni) nanoparticle colloidal solution was spin-coated at 2000 rpm, followed by annealing at 120 °C for 10 min. Afterwards, the aforementioned structure was transferred to an argon glove box for the preparation of the perovskite layer and the electron transport layer (ETL).

The perovskite precursor was obtained by dissolving 0.9 mol FAI, 1 mol PbI_2, 0.1 mol CsI, and 0.2 mol MACl in a 1 mL mixture solution of 4 : 1 V/V DMF/DMSO. The precursor was spin-coated according to a two-step process at 1000 rpm for 6 s and 3000 rpm for 35 s; 100 μl CB was added 5 s before the end of the second step. Then, the precursor film was heated at 100 °C for 20 min on a hotplate. For "sandwich" perovskite films, a solution of QDs with optimal concentration was pre-spin-coated on the HTL, and then the surface was rinsed sequentially with a saturated methyl acetate solution of lead acetate and methyl acetate solution. 70 μL perovskite precursor solution was added onto the pre-deposited QDs film and spin-coated at 1000 rpm for 6 s, followed by 3000 rpm for 35 s. During the last 5 s of the spin-coating process, 100 μL QD solution with optimal concentration was added onto the surface of the perovskite precursor during spin-coating. After the spin-coating process, the substrate was transferred to a 100 °C hot plate and annealed for 20 min. On top of the perovskite, the ETL of PCBM and BCP was spin-coated at 1500 rpm. Finally, a 100 nm-thick Ag electrode was deposited in a thermal evaporator, and then the LWUF PSC was removed from the glass/PDMS rigid substrate to complete the fabrication process. The LWUF PSC fabrication process is schematically shown in Fig. 1a.

2.4 Characterization of materials and devices

The morphology of the materials was characterized by field-emission scanning electron microscopy (SEM, Hitachi S5200) and high-resolution transmission electron microscopy (HR-TEM). The transmission and absorption spectra of the materials were recorded using an ultraviolet-visible-near infrared spectrophotometer (UV-3600, Shimadzu). Photoluminescence (PL) spectra were recorded using a LabRAM HR800 (HORIBA Jobin Yvon Inc.) with an excitation laser of 514 nm wavelength. Transient photocurrent (TPC) decay curves were generated by a microsecond pulse under short circuit conditions (by a very

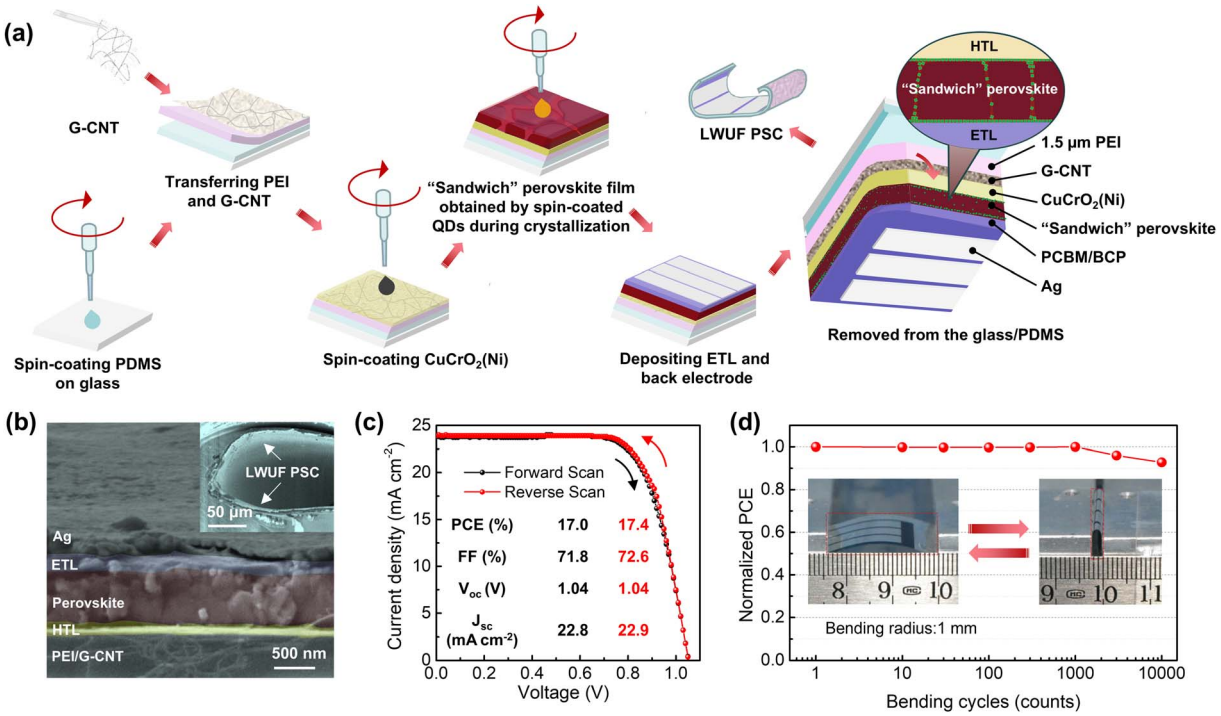

Fig. 1 The process routes and the structural and performance characteristics of the LWUF PSCs. (a) Schematics of the fabrication procedure. (b) Cross-sectional SEM image of the LWUF PSC. The inset shows the SEM image of a LWUF PSC under bending with a curvature radius of 70 μm. (c) *J*–*V* curves of the device, recorded in reverse scanning and forward scanning. (d) Mechanical stability of the devices at a bending radius of 1 mm. The inset in (d) shows the digital image of a device under bending cycles.

low resistor at 20 Ω). The sheet resistance of the G-CNT film was determined using a handheld four-probe meter (Tonghui, TH2661). The water contact angle was measured using an optical contact angle meter (OCA25, Dataphysics). The phase purity and crystal structure were identified by X-ray diffraction (XRD, Bruker, D8 Advance). Young's modulus of the perovskite films was obtained using an atomic force microscope (AFM, Bruker MultiMode-8 ScanAsyst). Space-charge-limited current (SCLC) and current density–voltage (*J–V*) characteristics were measured using a Keithley 4200-SCS. The *J–V* hysteresis curves were obtained in the reverse scan (from 1.2 V to −0.5 V, step 0.01 V) and forward scan (from −0.5 V to 1.2 V, step 0.01 V) under AM 1.5G (100 mW cm^{-2}) irradiation based on a solar simulator (CHF-XM 500, Beijing Trusttech Co. Ltd). Before J-V measurements, the simulator was cautiously calibrated by using a standard monocrystalline silicon solar cell. To ensure accuracy, a mask with a round aperture (the area is about 0.115 cm^2) was employed during the measuring process. The bending cycle test was performed using a stretching machine with a metal stand of specific outside diameter. The environmental stability test was performed at 25 °C in the ambient atmosphere, and the relative humidity (RH) was about 35%. All devices are not encapsulated in any way. Electrochemical impedance spectroscopy (EIS) was carried out on an electrochemical workstation (Zahner, IM6ex). The EIS measurements were performed over a frequency range of 1 MHz to 1 Hz with an applied amplitude of 5 mV. All tests used were conducted at ambient temperature under a normal atmospheric atmosphere.

3. Results and discussion

3.1 The overall excellent performance of the as-designed LWUF PSCs

The LWUF PSC, shown in the schematic diagram in Fig. 1a, results in high performance and excellent stability by adopting a collaborative approach to improve the performance of the FPSC. Specifically, the design scheme mainly includes the following four aspects: (1) a freestanding, ultra-light, very flexible and highly transparent conductive G-CNT film as the electrode; (2) a 1.5 μm-thick PEI film as the flexible substrate; (3) an optimized HTL to improve the device's efficiency; (4) a "sandwich" architecture composed of $CsPbBr_3$ QDs/polycrystalline perovskite mixed $CsPbBr_3$ QDs/$CsPbBr_3$ QDs for the first time as the light-absorbing layer. This approach not only improves the device's PCE but also reduces the weight of the device and improves its mechanical stability and environmental stability.

The entire fabrication process of the LWUF PSC is performed on a glass/PDMS rigid substrate, as shown in Fig. 1a. PDMS is used as an adhesive contact layer between the ultra-thin PEI and the rigid glass substrate to ensure neither wrinkling nor folding during the fabrication process and to facilitate the removal of the LWUF PSC from the rigid substrate. The detailed process steps are described in "2.3 Fabrication of solar cells". The entire LWUF PSC is configured as 1.5 μm-thick PEI/G-CNT/$CuCrO_2$(-Ni)/"sandwich" perovskite/PCBM/BCP/Ag, and its SEM image in Fig. 1b shows the cross-sectional structure. The inset shows the device under the bending state at a radius of curvature of about 70 μm, where the device's structure is intact and signifies great flexibility. In contrast, compared to the conventional FPSC prepared on 125 μm-thick PET, the cell structure has been severely disrupted at the same state (Fig. S2).

Fig. 1c shows the *J–V* curves for the forward and reverse scans of the LWUF PSC. The results show that the *J–V* curves in forward and reverse scans largely overlap, which indicates negligible hysteresis. The short-circuit current density (J_{SC}), open-circuit voltage (V_{OC}), and fill factor (FF) of the device in reverse scan are 22.9 mA cm^{-2}, 1.04 V, and 72.6%, respectively, which results in an optimal PCE of 17.4%. The weight of the 2.5 cm × 2.5 cm device is only 3.53 mg (areal density of 5.6 g m^{-2}), corresponding to 3.4% and 0.2% of conventional flexible and rigid devices, respectively (Fig. S3), which finally makes the power-per-weight reach 31.1 W g^{-1}. The currently reported FPSCs, fabricated on 1.3–57 μm-thick substrates, have an areal density of 4.4–71 g m^{-2} and a power-per-weight of 47.8–1.96 W g^{-1} (summarized in Table S1).[1,10–18] It is evident that, under the premise of considering the stability of the devices, the LWUF PSC prepared in this study is one of the few devices that can operate stably in air, and it also leads in terms of lightweight design among such stable devices. The mechanical flexibility of the LWUF PSC was tested by bending cycles with a curvature radius of 1 mm, as shown in Fig. 1d. The results showed that the device's PCE remained at 92.8% of the initial value after 10 000 bending cycles, exhibiting extreme mechanical flexibility.

3.2 Enhancement effect of freestanding and ultra-light G-CNT films on the flexibility and stability of LWUF PSCs

Using carbon nanofilms instead of metal oxides as the electrodes of PSCs can effectively improve the flexibility and stability of the device. G-CNT films were prepared by growing graphene to fill holes in a self-supporting continuous CNT network. So, the G-CNT film combines the self-supporting property of the CNT film with the densification of the graphene film, which is expected to further improve the FPSC's performance. The SEM and HR-TEM images of the G-CNT film in Fig. 2a show that the pores of the CNT network film formed by the intersection of CNT bundles through "X" and "Y" nodes are filled completely by the grown graphene, which significantly improves the moisture resistance of the G-CNT film. To compare the moisture resistance of CNT and G-CNT films in a humid environment, a drop of deionized water was placed on the surface of the copper foils covered with G-CNT and CNT films, respectively, and then heated to 80 °C to accelerate the corrosion of the copper foils below by moisture, as shown in Fig. 2b. After 10 min, red traces were observed in the dripping region on CNT/Cu, while no change was observed in the corresponding position on G-CNT/Cu. Under an optical microscope, patches of red cuprous oxide were observed at the trace site on CNT/Cu, but almost none on G-CNT/Cu. In previous reports, CNT film electrodes were considered effective in blocking moisture to improve PSC stability, so the as-grown G-CNT films are undoubtedly more likely to improve the device's stability.[22,34–36] The environmental stability of the device will be discussed in Section 3.4.

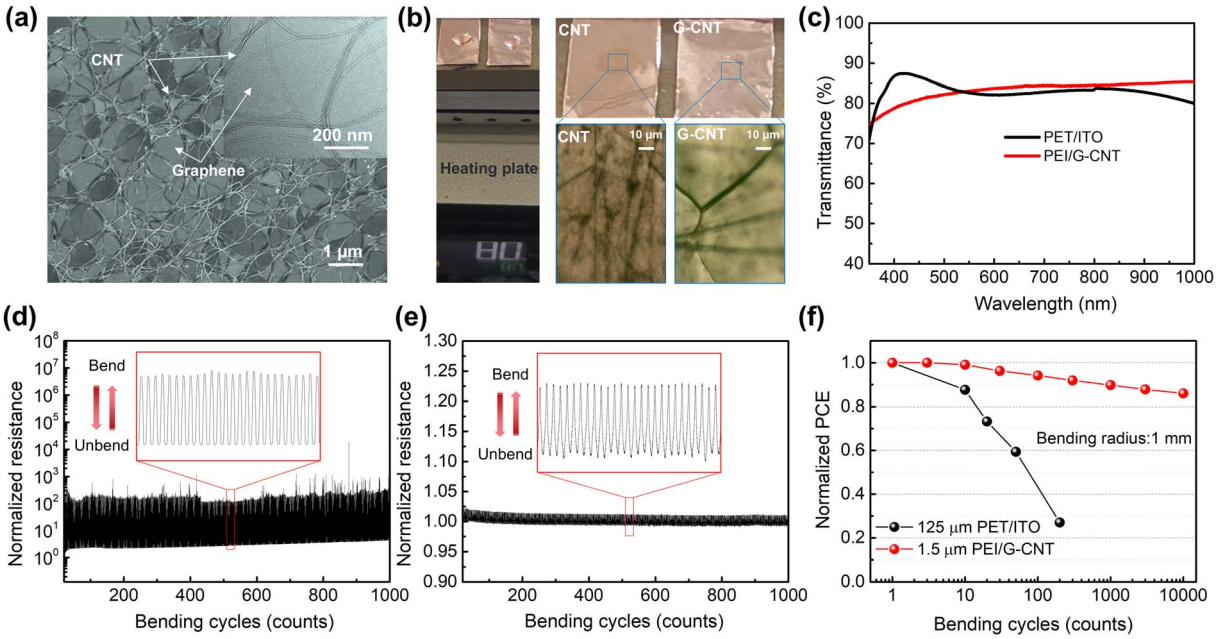

Fig. 2 The microstructure of a G-CNT film and its advantages as a flexible electrode. (a) SEM image of a G-CNT film. The inset shows its HR-TEM image. (b) Moisture resistance investigation of CNT and G-CNT films. (c) Transmittance of PEI/G-CNT and PET/ITO electrode substrates. The dynamic resistances of PET/ITO (d) and PEI/G-CNT (e) electrode substrates in real time during bending cycles with a 1 mm bending radius. (f) Normalized PCE of FPSCs based on PET/ITO and PEI/G-CNT electrode substrates as a function of bending cycles with a bending radius of 1 mm.

In addition, the as-grown G-CNT film presents excellent transparency, high conductivity, and outstanding flexibility.[37] In this study, PEI/G-CNT electrode substrates with a light transmittance of about 87% shown in Fig. 2c and a sheet resistance of about 100 Ω sq^{-1} are used. Although the electrical conductivity of the PEI/G-CNT flexible electrode substrate is not as good as that of the current commercial PET/ITO electrode substrate (with a sheet resistance of about 32 Ω sq^{-1}), the excellent mechanical flexibility of the PEI/G-CNT electrode substrate is something that the PET/ITO electrode substrate cannot match. The dynamic resistances of PET/ITO and PEI/G-CNT electrode substrates were monitored in real time during bending cycles with a bending radius of 1 mm in Fig. 2d and e, respectively. The results show that the resistance of a PET/ITO electrode substrate increases by two orders of magnitude from the straightened state to the bent state due to the fragility of ITO, while the increase in the resistance of a PEI/G-CNT electrode substrate is negligible. After 1000 bending cycles, the resistance of the PET/ITO electrode substrate has increased to 10 times its initial value (from about 32 Ω sq^{-1} to about 320 Ω sq^{-1}), while the corresponding change in that of the PEI/G-CNT electrode substrate is less than 2% (from about 100 Ω sq^{-1} to about 102 Ω sq^{-1}, which is only one-third of that of the PET/ITO electrode, revealing much higher dynamic conductivity). This indicates that the latter exhibits superior mechanical flexibility and excellent stable electrical conductivity during dynamic changes compared to the former.

In order to cope with more severe mechanical deformation, the G-CNT electrodes were also tested under winding, twisting, and stretching. The test results are shown in Fig. S4, indicating that this electrode has excellent tolerance to deformation. The weight of the 2.5 cm × 2.5 cm ultra-thin PEI/G-CNT electrode substrate is only 3.38 mg, and the surface density is less than 0.54 mg cm^{-2}, which is the main reason for making the as-designed LWUF PSC lightweight. The mechanical robustness of the devices with PET/ITO and PEI/G-CNT electrode substrates is compared in Fig. 2f. The device with a 1.5 μm-thick PEI/G-CNT electrode substrate is proven to retain about 86.2% of the initial PCE after bending 10 000 times at a curvature radius of 1 mm, while the corresponding device with a 125 μm-thick PET/ITO electrode substrate can only maintain 27% of the initial PCE after 200 bends. The improvement in the performance of the G-CNT-based device can be attributed to the superior electrical stability, water vapor barrier property, and mechanical flexibility of the G-CNT electrode, which collectively contribute to a slower rate of performance degradation during operation, thereby providing greater possibilities for large-scale applications. However, despite these advantages, the large-scale fabrication of G-CNT films is still in the development stage, as achieving uniform large-area G-CNT films continues to pose technical challenges that hinder their widespread adoption in FPSCs.

3.3 Optimization of the device's efficiency by $CuCrO_2$(Ni) nanoparticles as a HTL

As a high-conductivity organic polymer, PEDOT:PSS can have a synergistic effect with carbon nanofilms to improve the hole collection efficiency of solar cells.[38] In inverted PSCs, the balance between the work function and conductivity of PEDOT:PSS, as well as the high hygroscopicity, severely hinders the improvement of the device's PCE and long-term stability.[39,40]

An effective approach involves the doping modification of PEDOT:PSS or identifying novel HTL materials to address the interfacial contact issues with perovskite films. $CuCrO_2$ nanoparticles, as an inorganic HTL material, exhibit excellent water dispersibility and tunable optoelectronic properties.[31,41] However, the relatively low crystalline quality of this material limits its direct application in high-efficiency PSCs.[42,43] In this study, we synthesized a high-quality $CuCrO_2$(Ni) HTL by introducing nickel into $CuCrO_2$ nanoparticles. Structural and morphological characterization (as shown in Fig. S1) confirmed that the material possesses a hexagonal 2H–$CuCrO_2$ crystal structure with an average grain size of 10–15 nm. Compared with previously reported $CuCrO_2$ nanoparticles,[42,43] the $CuCrO_2$(Ni) nanoparticles prepared in this work exhibit higher crystallinity (Fig. S1a) and more efficient photogenerated charge extraction and transport capabilities (Fig. S5), which are expected to result in improved performance in PSCs.

Fig. 3a shows the *J*–*V* curves of the PSCs on the rigid glass/G-CNT electrode substrates with different HTLs. The results demonstrate that after using the $CuCrO_2$(Ni) HTL, the V_{OC} and FF of the device increase from 1.04 V and 63.9% to 1.09 V and 72.2%, respectively, and the PCE of the cell increases from 15.4% to 18.4%, an increase of 20%. The enhancement of the device's photovoltaic performance is attributed to the improved carrier transport at the interface. To substantiate this, we analyzed the PL spectra of perovskite films deposited on PEDOT:PSS and $CuCrO_2$(Ni) HTLs. From the PL spectra (Fig. 3b), it can be found that the perovskite on the $CuCrO_2$(Ni) HTL has a weaker PL peak, which indicates that the photoquenching is more pronounced than that deposited on the PEDOT:PSS HTL.[22] TPC is a common technique for analyzing the carrier lifetime of materials, and the carrier lifetime can be directly calculated by fitting the TPC curve with a double exponential function. Fig. 3c shows that the carrier lifetimes of the perovskite on the two HTLs are 116 ns and 57 ns, respectively. The shorter carrier lifetime of the $CuCrO_2$(Ni) structure indicates that the separation and transport efficiency of photogenerated carriers in perovskite are improved, which is also the reason for the more significant PL spectra quenching of this structure. We further performed Mott–Schottky analysis to gain more insight into the effect of the $CuCrO_2$(Ni) HTL on carrier diffusion and extraction within the perovskite. The built-in potentials (V_{bi}) can be estimated by fitting the C^{-2}–V linear relationship according to eqn (1):[44]

$$C^{-2} = \frac{2}{NA^2q\varepsilon\varepsilon_0}(V_{bi} - V) \quad (1)$$

where C is the capacitance, V is the applied voltage, N is the defect density, A is the device's area, q is the elementary charge, ε is the relative dielectric constant of the perovskite material (ε = 46.9 for $FAPbI_3$),[45] and ε_0 is the vacuum permittivity (8.8542×10^{-12} F m^{-1}). As shown in Fig. 3d, the V_{bi} for the PSC with the $CuCrO_2$(Ni) HTL is 0.91, significantly higher than that of the PSC with the PEDOT:PSS HTL. A higher V_{bi} signifies the formation of a stronger electric field in the PSC, which favors carrier transfer.[46] Furthermore, the corresponding carrier density at the perovskite interface is inversely proportional to the slope of the C^{-2}–V fitted line.[9] The lower line slope of the device based on the $CuCrO_2$(Ni) HTL refers to the higher interfacial carrier density, which suggests that more carriers in the perovskite of the device have been separated and transported. This is in good agreement with the weak PL intensity and the short carrier lifetime of the composite HTL structure.

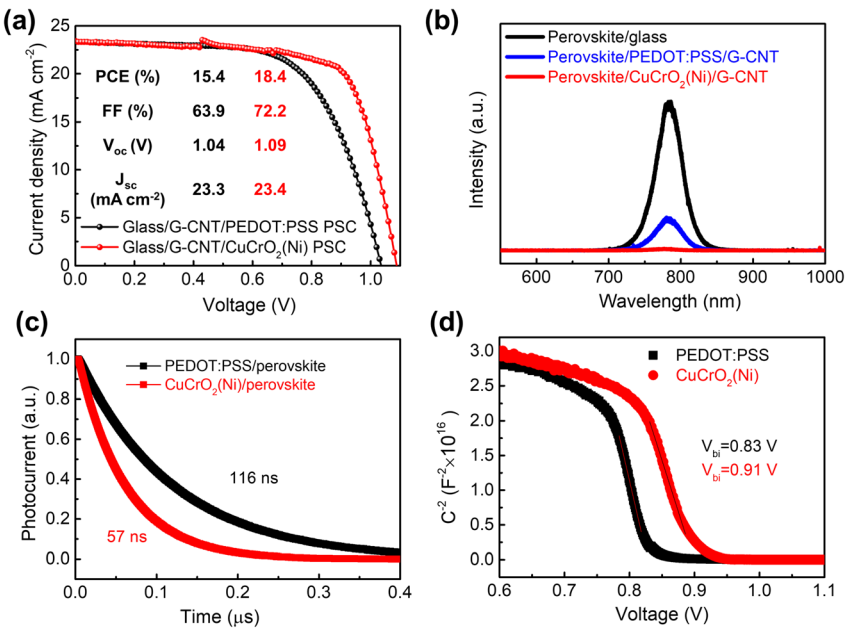

Fig. 3 Optimization of the device's efficiency using $CuCrO_2$(Ni) nanoparticles. (a) *J*–*V* curves of the PSCs on rigid glass/G-CNT electrode substrates with different HTLs. (b) PL spectra. (c) TPC curves. (d) The Mott–Schottky analysis plot.

3.4 Excellent flexibility, marked stability and high PCE of the LWUF PSC enabled by the "sandwich" perovskite

It is noted that in recent years, perovskite QDs (such as $CsPbBr_3$ QDs) have been applied to interface modification materials and light absorption materials in PSCs,[28,47] effectively improving the flexibility of PSCs, although their PCE is much lower than that of rigid PSCs. In this study, we intend to combine the advantages of perovskite QDs and polycrystalline perovskite and try to adopt a scheme to refine polycrystalline perovskite grains, to jointly improve the flexibility and PCE of PSCs.

We design a "sandwich" perovskite architecture as a light absorption layer for the first time. The grain size of the as-synthesized $CsPbBr_3$ QDs is about 20 nm. Their structural characterization by HR-TEM and XRD is shown in Fig. S6. "Sandwich" perovskite layers were prepared by burying bottom QDs before crystallization and then spin-coating QDs on the upper surface of polycrystalline perovskite during crystallization. The SEM images in Fig. 4a and b show that the polycrystalline perovskite consists of uneven and large grains with diameters ranging from 200 nm to 1000 nm (Fig. 4a and a′), with gaps and pinholes at the wider grain boundaries, while the "sandwich" perovskite consists of small grains with diameters of 100–200 nm (Fig. 4b and b′) packed to form a dense structure. The smaller grain size and denser structure of the "sandwich" film compared to the polycrystalline film are attributed to the modulation effect of QDs. The SEM images of the "sandwich" perovskite films with different QDs are shown in Fig. S7 and S8. The film with 5 mg mL^{-1} QDs exhibits relatively uniform grain shapes and sizes and a dense structure, so we use this concentration to regulate the formation of perovskite. The QDs incorporated during the crystallization process act as nucleation sites for perovskite crystallization and promote grain refinement. Comparing Fig. 4a′, b′ and S7, it can be seen that when the QDs are first buried at the bottom the perovskite crystal particles on the HTL tend to be smaller and more dense than those without adding QDs, and this modulation effect is

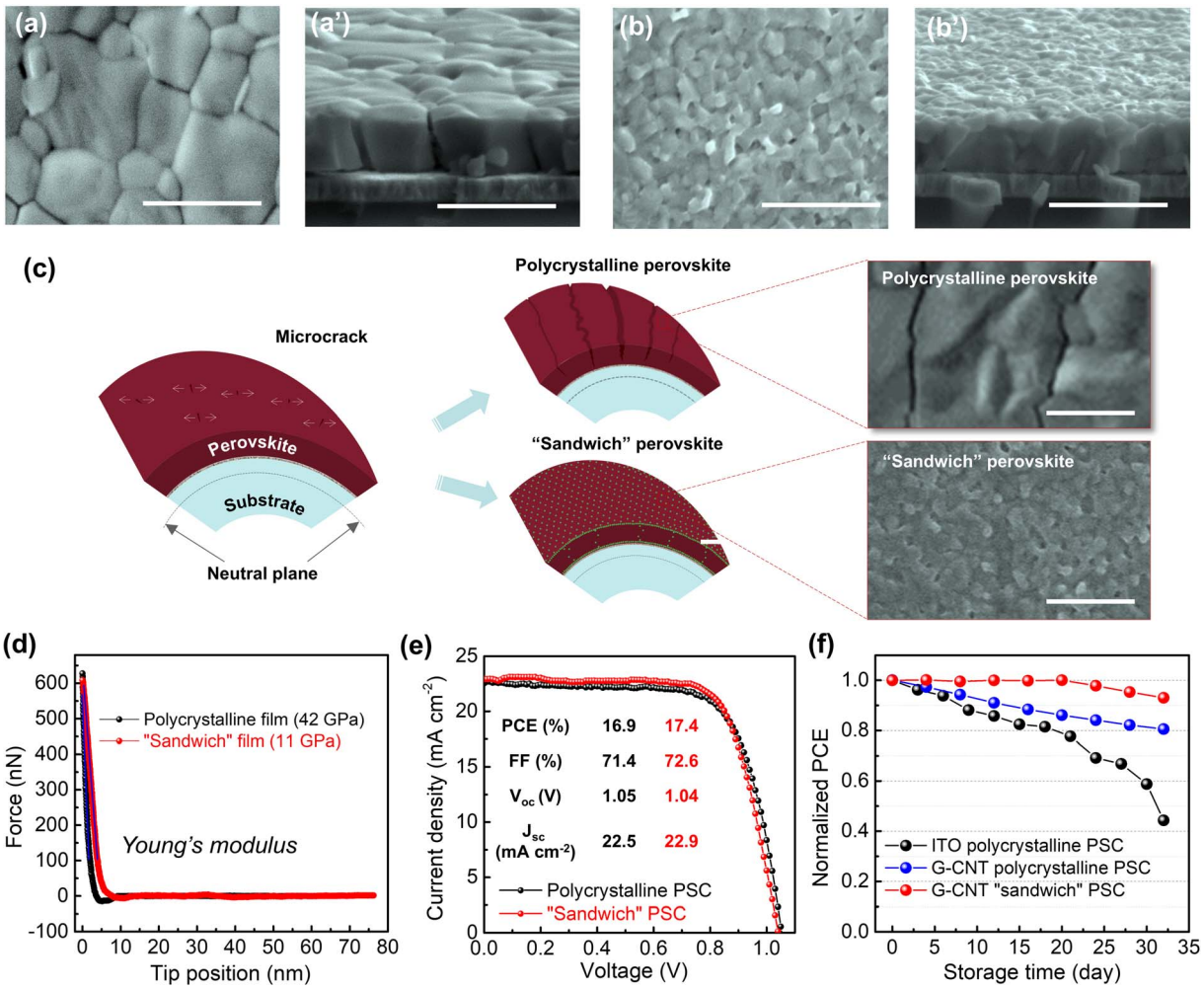

Fig. 4 Improvement of the device's performance by the as-designed "sandwich" perovskite architecture. The SEM images of the top and cross-section of the polycrystalline perovskite film (a and a′) and the "sandwich" perovskite film (b and b′). (c) Schematic representation of the relationship between the perovskite structure and the cracks generated during bending. The inset shows SEM images of two kinds of perovskite films after 1000 bending cycles at a curvature radius of 4 mm. (d) Young's modulus of polycrystalline and "sandwich" films. (e) *J*–*V* curves of LWUF PSCs. (f) Environmental stability of the PSCs. The scale bar is 1 μm.

more obvious in the crystallization process of the middle layer of the "sandwich" and the addition of quantum dots at the top. If only QDs are laid on the HTL, but no QDs are added in the subsequent perovskite crystallization, the particles on the upper surface of the perovskite layer are still uneven and large in size, as shown in Fig. S9.

The XRD diffraction pattern in Fig. S10 shows that the "sandwich" perovskite synthesized by adding QDs retains the crystal structure of the polycrystalline perovskite film, which may be related to the position of QDs in the polycrystalline film. According to the EDS mapping (Fig. S11), cesium is mainly distributed around the grain. Since cesium atoms mainly exist in QDs, it can be concluded that QDs occupy the grain boundary of the polycrystalline film, which may also be the reason for retaining the crystal structure of the polycrystalline film. The QDs entering the grain boundaries of the polycrystalline films will also fill the voids and pinholes, leading to densification of the films.

In order to verify the flexibility of the two perovskites (*i.e.*, the polycrystalline perovskite and the "sandwich" perovskite), they were deposited onto a normal 125 μm-thick PET, respectively. Their surface morphologies were compared after bending 1000 times with a curvature radius of 4 mm. As shown in Fig. 4c, the "sandwich" perovskite layer did not exhibit some cracks as the polycrystalline perovskite layer did. To figure out why "sandwich" perovskite does not crack, the Young's modulus of two perovskite and QD films was measured using the peak-force model of AFM, as shown in Fig. 4d and S12.[48] The results show that the Young's modulus of the "sandwich" perovskite is 11 GPa, higher than the 8 GPa of QDs and lower than the 42 GPa of the polycrystalline film. The lowest Young's modulus of QDs can be attributed to their small particle size and the soft surface ligands between particles,[28] which may facilitate interparticle motion and thus contribute to the excellent flexibility of QDs. These results allow us to conclude that the QDs filled at grain boundaries act as a "roller" during the bending process, effectively promoting the inter-grain sliding and preventing the formation of micro-cracks after deformation. Similarly, the "sandwich" perovskite has a significantly lower Young's modulus than the polycrystalline film, meaning that it may be able to withstand more elastic deformation to release stress under the same pressure, which helps stabilize the crystal structure under deformation to prevent cracking.

Naturally, LWUF PSCs were further prepared on ultra-thin PEI/G-CNT electrode substrates using polycrystalline and "sandwich" perovskites, respectively. The *J–V* curves and performance parameters of the two devices are shown in Fig. 4e. The PCE of the "sandwich" device increases to 17.4%, compared to 16.9% for the polycrystalline LWUF PSC. The reproducibility of the study results shows that the arithmetic mean (M) of the PCE of the "sandwich" device group increases to 17.1% from 16.5% of the control group, and the standard deviation (σ) decreases to 0.269 from 0.302 of the control group (Fig. S13), indicating that the "sandwich" LWUF PSC has higher PCE and repeatability. The mechanical robustness of the resultant devices can be seen in Fig. S14. After 10 000 bending cycles with a curvature radius of 1 mm, the "sandwich" perovskite-based LWUF PSC retains 92.8% of its initial PCE, while the polycrystalline perovskite LWUF PSC maintains 86.2% of its original PCE. Thus, thanks to the structural design of the "sandwich" perovskite layer combined with the G-CNT flexible electrode, the "sandwich" perovskite LWUF PSC exhibits superior efficiency and excellent mechanical stability.

As another key indicator for evaluating the device's performance, its environmental stability was measured in a dark environment with 35% RH and 25 °C, as shown in Fig. 4f. For the polycrystalline PSC fabricated with G-CNT instead of the ITO electrode, the PCE retention rate increased from 44.3% to 80.6% after 32 days. This remarkable improvement is attributed to the excellent moisture resistance of the G-CNT films (Fig. S15). Moreover, the environmental stability of the "sandwich" perovskite-based PSC is significantly superior to that of the polycrystalline perovskite-based PSC, further indicating that QD passivation can also improve the environmental stability of PSCs. This is because the surface coordination of QDs contains a large number of alkane functional groups.[49] When they are anchored at the grain boundaries and the surface of perovskite, a non-polar molecular hydrophobic layer will be formed on its surface (Fig. S16). Ultimately, the as-designed "sandwich" perovskite-based LWUF PSC with G-CNT electrodes presented the best environmental stability, as the device maintained 93.0% of the initial PCE after 32 days.

The "sandwich" devices on flexible PEI/G-CNT electrode substrates demonstrate effective performance enhancement, which should be related to the carrier behavior in the "sandwich" perovskite layer. Then, PL, SCLC and EIS tests were carried out to investigate the carrier recombination dynamics. The PL intensity of the "sandwich" perovskite film is slightly higher than that of the polycrystalline film (Fig. 5a), implying that the QD-based passivation process in the "sandwich" perovskite does not lead to an increase in defect density despite grain refinement. This highlights the effectiveness of QDs in passivating perovskite defects, which is similar to the findings reported in the literature,[49] where post-treatment of crystallized perovskite surfaces with QDs was demonstrated to reduce defect density and enhance PL emission. According to the SCLC results in Fig. 5b, the trap-filled limit voltages (V_{TFL}) of the "sandwich" perovskite-based device and the polycrystalline perovskite-based device are 0.26 V and 0.32 V, respectively. The trap state density (n_{t}) used to quantify the concentration of defects can be calculated according to eqn (2):[50]

$$n_{\mathrm{t}} = \frac{2\varepsilon\varepsilon_0 V_{\mathrm{TFL}}}{qd^2} \quad (2)$$

where d is the film thickness. Compared with the polycrystalline perovskite-based device, the n_t of the "sandwich" perovskite device slightly decreases from 7.67×10^{21} m^{-3} to 6.23×10^{21} m^{-3} (as shown in Table S2), indicating that the defect density in "sandwich" perovskite is not higher or even lower than that of polycrystalline perovskite. Based on previous findings, the weak interaction between the carbonyl group on the QD ligand and Pb allows the QDs to be chemically anchored at the grain boundaries.[47,51] A similar phenomenon is observed, where "sandwich" perovskites exhibit a unique structure in which QDs

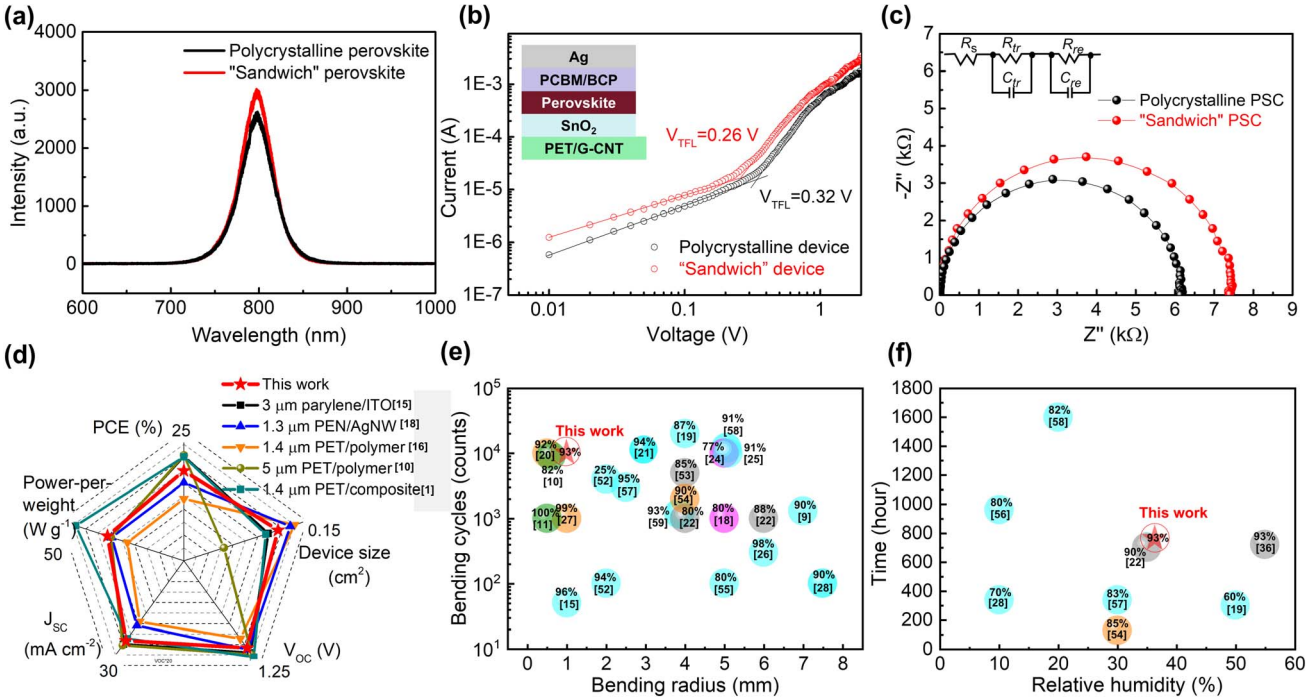

Fig. 5 Performance of LWUF PSCs based on polycrystalline and "sandwich" perovskite films. (a) PL spectra of perovskite films. (b) SCLC measurements. (c) Nyquist plots. The insets in (b) and (c) show the electron-only device's architecture and equivalent circuit model, respectively. (d) Comparison of the performance of the LWUF PSC in this work with that of FPSCs reported so far. (e) Mechanical stability of the FPSCs reported so far. (f) Environmental stability of the FPSCs reported so far. Light blue, magenta, gray, and saffron yellow bubbles in (e) and (f) represent ITO electrodes, Ag nanowire electrodes, carbon nanofilm electrodes, and composite electrode-based FPSCs in that order, and the percentages on the bubbles represent the retention rate of PCE after bending or aging.

are incorporated into the pinholes and grain boundaries of polycrystalline perovskites (Fig. S10 and S11). Therefore, the experimental results suggest that the QDs entering pinholes and grain boundaries of the "sandwich" perovskite may also be able to passivate defects.

Fig. 5c presents the Nyquist plot of devices with polycrystalline perovskite and "sandwich" perovskite under dark conditions. The inset shows the equivalent circuit model, composed of series resistance (R_S), transfer resistance (R_{tr}), recombination resistance (R_{re}), and parallel capacitance.[44] The fitting parameters are shown in Table S3. Compared to the polycrystalline perovskite-based device, R_{re} of the "sandwich" perovskite-based device increases from 5644 Ω to 6917 Ω and R_{tr} decreases from 295 Ω to 242 Ω (R_s change can be neglected), which shows that the carrier recombination in the device is effectively suppressed due to defect passivation, thereby increasing the V_{OC} and FF of devices.

In addition, our work provides an effective approach to fabricate LWUF PSCs on an ultra-thin PEI/G-CNT electrode substrate. Among these LWUF PSCs, the as-designed "sandwich" perovskite exhibits three functions in improving the device's performance: ① By forming uniform and fine grains on the surface of the perovskite, it enhances the flexibility of the perovskite film and thereby improves the device's mechanical stability. ② By passivating the interface defects of the perovskite with QDs, it is conducive to increasing the PCE of the device. ③ Meanwhile, due to the passivation effect of QDs, by forming hydrophobic layers at the grain boundaries and on the surface, it undoubtedly helps to enhance the environmental stability of LWUF PSCs.[49] Thus, the resultant device contributes a high efficiency of 17.4% and a power-per-weight of 31.1 W g^{-1}, which is also the highest performance reported so far for LWUF PSCs with inorganic nanofilm electrodes, as shown in Fig. 5d (detailed results are summarized in Table S1).[1,10,15,16,18] Furthermore, the mechanical flexibility and environmental stability of the resultant device are at the top level among the FPSC devices reported previously, as shown in Fig. 5e and f (detailed results are summarized in Tables S4 and S5).[9–11,15,18–22,24–28,36,52–59] These results will further promote the application of FPSCs in fields such as wearable devices, flexible electronics, artificial intelligence robots, aerospace and so forth.

4. Conclusions

In this study, a LWUF PSC with high performance and excellent stability has been fabricated by adopting a collaborative approach in terms of four aspects. First, selecting a free-standing, ultra-light, very flexible and highly transparent conductive G-CNT film as the electrode, instead of the conventional oxide electrode, has improved the flexibility, mechanical stability and environmental stability of PSCs. Second, using a 1.5 μm-thick PEI film as a flexible substrate has increased flexibility and reduced the weight of the device

greatly. Third, optimizing the transfer of photogenerated charge carriers by employed $CuCrO_2$(Ni) nanoparticles as a novel HTL has boosted the PCE of PSCs. Fourth, a "sandwich" perovskite layer of $CsPbBr_3$ QDs wrapped around the compact perovskite grains is designed as a light absorption layer with synergistic effects for the first time, giving the LWUF PSC excellent flexibility, remarkable stability and high PCE. As a result, the resultant device records a PCE of 17.4% and a power-per-weight of 31.1 W g^{-1}, which is the best performance of LWUF PSCs with nanofilm electrodes to date. In addition, the formation of sandwich-structured perovskite films through QD passivation effectively addresses the issue of deteriorated interfacial contact behavior resulting from the limited mechanical supportability of ultrathin substrates. The grain size of the "sandwich" perovskite decreased from random 200–1000 nm to uniform 100–200 nm. Moreover, the QDs introduced at the grain boundaries and surfaces acted as rollers for grain sliding during deformation, effectively suppressing the cracking problem after bending. As a result, the LWUF PSCs retained 92.8% of the initial PCE after 10 000 bending cycles with a curvature radius of 1 mm. Due to the use of an impermeable "sandwich" perovskite absorption layer and a G-CNT electrode, the LWUF PSC maintains 93.0% of its initial PCE after 32 days in an atmosphere of 35% RH, presenting excellent environmental stability. Given the high PCE, power-per-weight, outstanding mechanical flexibility, and marked environmental stability of this LWUF PSC, it is expected to meet a wider range of needs and applications, such as wearable devices, flexible electronics, and aerospace applications.

Conflicts of interest

There are no conflicts to declare.

Data availability

The data supporting this article have been included as part of the SI.

Supplementary information is available. See DOI: **https://doi.org/10.1039/d5ta06002h**.

Acknowledgements

This work was supported by the National Key R&D Program of China (Grant No. 2024YFA1210602 and 2020YFA0714700) and the National Natural Science Foundation of China (Grant No. 52172060, 12474179, and 51820105002). Prof. X. J. Wei thanks the Youth Innovation Promotion Association of the Chinese Academy of Sciences (Grant No. 2020005) and One Hundred Talent Project of Institute of Physics, CAS. Prof. H. P. Liu and Prof. X. Zhang acknowledge support from the "One Hundred Talents Project" of CAS.

References

1 B. Hailegnaw, S. Demchyshyn, C. Putz, L. E. Lehner, F. Mayr, D. Schiller, R. Pruckner, M. Cobet, D. Ziss, T. M. Krieger, A. Rastelli, N. S. Sariciftci, M. C. Scharber and M. Kaltenbrunner, *Nat. Energy*, 2024, **9**, 677–669.
2 Y. Gao, K. Huang, C. Long, Y. Ding, J. Chang, D. Zhang, L. Etgar, M. Liu, J. Zhang and J. Yang, *ACS Energy Lett.*, 2022, **7**, 1412–1445.
3 P. Jiang, J. Chen, F. Qin, T. Liu, S. Xiong, W. Wang, C. Xie, X. Lu, Y. Jiang, H. Han and Y. Zhou, *Angew. Chem., Int. Ed.*, 2022, **61**, e202208815.
4 S. Cho, D. Jung, J. Kim, J. Seo, H. Ju and J. Lee, *Adv. Mater. Technol.*, 2022, **7**, 2200344.
5 T. S. Kim, H. J. Kim, D. M. Geum, J. H. Han, I. S. Kim, N. Hong, G. H. Ryu, J. Kang, W. J. Choi and K. J. Yu, *ACS Appl. Mater. Interfaces*, 2021, **13**, 13248–13253.
6 M. Kaltenbrunner, M. S. White, E. D. Glowacki, T. Sekitani, T. Someya, N. S. Sariciftci and S. Bauer, *Nat. Commun.*, 2012, **3**, 770.
7 H. Kimura, K. Fukuda, H. Jinno, S. Park, M. Saito, I. Osaka, K. Takimiya, S. Umezu and T. Someya, *Adv. Mater.*, 2019, **31**, e1808033.
8 W. Song, K. Yu, E. Zhou, L. Xie, L. Hong, J. Ge, J. Zhang, X. Zhang, R. Peng and Z. Ge, *Adv. Funct. Mater.*, 2021, **31**, 2102694.
9 Z. Zheng, F. Li, J. Gong, Y. Ma, J. Gu, X. Liu, S. Chen and M. Liu, *Adv. Mater.*, 2022, **34**, 2109879.
10 Z. Wang, Z. Lv, G. Liu, H. Li, S. Li, Y. Gao, H. Ma, Q. Dong, M. Pei, Z. Ying, Y. Yan and Y. Shi, *Adv. Funct. Mater.*, 2025, 09960.
11 G. Tang, F. Zheng, J. Song, Q. Tai, J. Zhao and F. Yan, *Adv. Sci.*, 2025, **12**, 2415372.
12 Z. Liu, P. You, C. Xie, G. Tang and F. Yan, *Nano Energy*, 2016, **28**, 151–157.
13 M. Xie, J. Wang, J. Kang, L. Zhang, X. Sun, K. Han, Q. Luo, J. Lin, L. Shi and C.-Q. Ma, *Flexible Printed Electron.*, 2019, **4**, 034002.
14 C. Jia, X. Zhao, Y.-H. Lai, J. Zhao, P.-C. Wang, D.-S. Liou, P. Wang, Z. Liu, W. Zhang, W. Chen, Y.-H. Chu and J. Li, *Nano Energy*, 2019, **60**, 476–484.
15 J. Wu, P. Chen, H. Xu, M. Yu, L. Li, H. Yan, Y. Huangfu, Y. Xiao, X. Yang, L. Zhao, W. Wang, Q. Gong and R. Zhu, *Sci. China Mater.*, 2022, **65**, 2319–2324.
16 M. Kaltenbrunner, G. Adam, E. D. Glowacki, M. Drack, R. Schwodiauer, L. Leonat, D. H. Apaydin, H. Groiss, M. C. Scharber, M. S. White, N. S. Sariciftci and S. Bauer, *Nat. Mater.*, 2015, **14**, 1032.
17 Y. Li, L. Meng, Y. Yang, G. Xu, Z. Hong, Q. Chen, J. You, G. Li, Y. Yang and Y. Li, *Nat. Commun.*, 2016, **7**, 10214.
18 S. Kang, J. Jeong, S. Cho, Y. J. Yoon, S. Park, S. Lim, J. Y. Kim and H. Ko, *J. Mater. Chem. A*, 2019, **7**, 1107–1114.
19 N. Jiang, B. Xing, Y. Wang, H. Zhang, D. Yin, Y. Liu, Y. Bi, L. Zhang, J. Feng and H. Sun, *Sci. Bull.*, 2022, **67**, 794–802.
20 U. Kim, M. Han, J. Jang, J. Shin, M. Park, J. Byeon and M. Choi, *Adv. Energy Mater.*, 2022, **13**, 2203198.
21 Z. Li, C. Jia, Z. Wan, J. Cao, J. Shi, J. Xue, X. Liu, H. Wu, C. Xiao, C. Li, M. Li, C. Zhang and Z. Li, *Nat. Commun.*, 2025, **16**, 1771.
22 J. Zhang, X. Hu, H. Li, K. Ji, B. Li, X. Liu, Y. Xiang, P. Hou, C. Liu, Z. Wu, Y. Shen, S. D. Stranks, S. R. P. Silva,

H. M. Cheng and W. Zhang, *Adv. Funct. Mater.*, 2021, **31**, 2104396.
23 G. Lee, M.-c. Kim, Y. W. Choi, N. Ahn, J. Jang, J. Yoon, S. M. Kim, J.-G. Lee, D. Kang, H. S. Jung and M. Choi, *Energy Environ. Sci.*, 2019, **12**, 3182–3191.
24 H. W. Zhang, Y. G. Bi, D. M. Shan, Z. Y. Chen, Y. F. Wang, H. B. Sun and J. Feng, *Nanoscale*, 2023, **15**, 5429–5436.
25 W. Zhang, J. Liu, W. Song, J. Shan, H. Guan, J. Zhou, Y. Meng, X. Tong, J. Zhu, M. Yang and Z. Ge, *Sci. Adv.*, 2025, **11**, eadr2290.
26 M. Karimipour, S. Khazraei, B. J. Kim, G. Boschloo and E. M. J. Johansson, *Nano Energy*, 2022, **95**, 107044.
27 R. Miao, P. Li, W. Zhang, X. Feng, L. Qian, J. Fang, W. Song and W. Wang, *Adv. Mater. Interfaces*, 2021, **9**, 2101669.
28 L. Hu, Q. Zhao, S. Huang, J. Zheng, X. Guan, R. Patterson, J. Kim, L. Shi, C. H. Lin, Q. Lei, D. Chu, W. Tao, S. Cheong, R. D. Tilley, A. W. Y. Ho-Baillie, J. M. Luther, J. Yuan and T. Wu, *Nat. Commun.*, 2021, **12**, 466.
29 S. Xiao, Q. Fan, X. Xia, Z. Xiao, H. Chen, W. Xi, P. Chen, J. Li, Y. Wang, H. Liu and W. Zhou, *Chin. Phys. B*, 2018, **27**, 078801.
30 Q. Zhang, W. Y. Zhou, X. G. Xia, K. W. Li, N. Zhang, Y. C. Wang, Z. J. Xiao, Q. X. Fan, E. I. Kauppinen and S. S. Xie, *Adv. Mater.*, 2020, **32**, 2004277.
31 Y. Li, H. Luo, L. Mao, L. Yu, X. Li, L. Jin and J. Zhang, *Adv. Mater. Interfaces*, 2021, **8**, 2100801.
32 S. Jeong, S. Seo and H. Shin, *RSC Adv.*, 2018, **8**, 27956–27962.
33 F. Li, S. Zhou, J. Yuan, C. Qin, Y. Yang, J. Shi, X. Ling, Y. Li and W. Ma, *ACS Energy Lett.*, 2019, **4**, 2571–2578.
34 M. Tian, C. Y. Woo, J. W. Choi, J. Y. Seo, J. M. Kim, S. H. Kim, M. Song and H. W. Lee, *ACS Appl. Mater. Interfaces*, 2020, **12**, 54806–54814.
35 Y. Yang, H. Chen, C. Hu and S. Yang, *J. Mater. Chem. A*, 2019, **7**, 22005–22011.
36 J. Zhang, X.-G. Hu, K. Ji, S. Zhao, D. Liu, B. Li, P.-X. Hou, C. Liu, L. Liu, S. D. Stranks, H.-M. Cheng, S. R. P. Silva and W. Zhang, *Nat. Commun.*, 2024, **15**, 2245.
37 Y. Yue, D. Zhang, P. Wang, X. Xia, X. Wu, Y. Zhang, J. Mei, S. Li, M. Li, Y. Wang, X. Zhang, X. Wei, H. Liu and W. Zhou, *Adv. Mater.*, 2024, **36**, 2313971.
38 Q. Fan, Q. Zhang, W. Zhou, X. Xia, F. Yang, N. Zhang, S. Xiao, K. Li, X. Gu, Z. Xiao, H. Chen, Y. Wang, H. Liu, W. Zhou and S. Xie, *Nano Energy*, 2017, **33**, 436–444.
39 Q.-D. Yang, J. Li, Y. Cheng, H.-W. Li, Z. Guan, B. Yu and S.-W. Tsang, *J. Mater. Chem. A*, 2017, **5**, 9852–9858.
40 D. S. Mann, Y.-H. Seo, S.-N. Kwon and S.-I. Na, *J. Alloys Compd.*, 2020, **812**, 152091.
41 S. Akin, Y. Liu, M. I. Dar, S. M. Zakeeruddin, M. Grätzel, S. Turan and S. Sonmezoglu, *J. Mater. Chem. A*, 2018, **6**, 20327–20337.
42 W. A. Dunlap-Shohl, T. B. Daunis, X. Wang, J. Wang, B. Zhang, D. Barrera, Y. Yan, J. W. P. Hsu and D. B. Mitzi, *J. Mater. Chem. A*, 2018, **6**, 469–477.
43 R.-J. Huang, S. Sakthinathan, T.-W. Chiu and C. Dong, *RSC Adv.*, 2021, **11**, 12607–12613.
44 J. Du, C. Qiu, S. Li, W. Zhang, W. Zhang, Y. Wang, Z. Qiu, Q. Wang, K. Yang, A. Mei, Y. Rong, Y. Hu and H. Han, *Adv. Energy Mater.*, 2022, **12**, 2102229.
45 K. Huang, Y. Peng, Y. Gao, J. Shi, H. Li, X. Mo, H. Huang, Y. Gao, L. Ding and J. Yang, *Adv. Energy Mater.*, 2019, **9**, 1901419.
46 W.-T. Wang, P. Chen, C.-H. Chiang, T.-F. Guo, C.-G. Wu and S.-P. Feng, *Adv. Funct. Mater.*, 2020, **30**, 1909755.
47 Y. Zhang, Z. Li, H. Chen, Y. Xu, Y. Lei, G. Peng, X. Zhou, Q. Wang and Z. Jin, *Adv. Mater. Interfaces*, 2022, **9**, 2200813.
48 T. J. Young, M. A. Monclus, T. L. Burnett, W. R. Broughton, S. L. Ogin and P. A. Smith, *Meas. Sci. Technol.*, 2011, **22**, 125703.
49 Y. Li, L. Duan, Z. Zhang, H. Wang, T. Chen and J. Luo, *Nano Res.*, 2023, **16**, 4888–4894.
50 Q. Han, S.-H. Bae, P. Sun, Y.-T. Hsieh, Y. Yang, Y. S. Rim, H. Zhao, Q. Chen, W. Shi, G. Li and Y. Yang, *Adv. Mater.*, 2016, **28**, 2253–2258.
51 J. Ge, W. Li, X. He, H. Chen, W. Fang, X. Du, Y. Li and L. Zhao, *Sustain. Energy Fuels*, 2020, **4**, 1837–1843.
52 Y. Lan, Y. Wang, Y. Lai, Z. Cai, M. Tao, Y. Wang, M. Li, X. Dong and Y. Song, *Nano Energy*, 2022, **100**, 107523.
53 J. Yoon, H. Sung, G. Lee, W. Cho, N. Ahn, H. S. Jung and M. Choi, *Energy Environ. Sci.*, 2017, **10**, 337–345.
54 H. Ji, J. Huang, W. Zhang, X. Chen, Y. Lu, C. Ding, J. Fang, W. Song and L. Ai, *Adv. Mater. Interfaces*, 2022, **9**, 2200483.
55 N. Zhu, X. Qi, Y. Zhang, G. Liu, C. Wu, D. Wang, X. Guo, W. Luo, X. Li, H. Hu, Z. Chen, L. Xiao and B. Qu, *ACS Appl. Energy Mater.*, 2019, **2**, 3676–3682.
56 Y. Zhu, L. Shu, S. Poddar, Q. Zhang, Z. Chen, Y. Ding, Z. Long, S. Ma, B. Ren, X. Qiu and Z. Fan, *Nano Lett.*, 2022, **2**, 9586–9595.
57 Z. Li, Z. Wang, C. Jia, Z. Wan, C. Zhi, C. Li, M. Zhang, C. Zhang and Z. Li, *Nano Energy*, 2022, **94**, 106919.
58 Y. Yang, N. Yang, C. Zhang, S. Li, Y. Hao, Q. Sun, Z. Chen, S. Liu, F. Guo, J. Lu and Y. Hao, *Adv. Sci.*, 2025, e08253.
59 S. Gao, X. Fan, J. Wang, F. Wei, J. Chen, X. Liu, J. Wang, H. Huang, J. Li, Z. Zhang, F. Yan and W. Song, *ACS Nano*, 2025, **19**, 28888–28899.